INVITED PAPER

Disturbance Propagation in Power Grids With High Converter Penetration

This article examines and discusses the influence of wave-like disturbance propagation by the high-level integration of converter-based resources in power networks.

By Hantao Cui, *Senior Member IEEE*, Stavros Konstantinopoulos, *Member IEEE*, Denis Osipov, *Member IEEE*, Jinning Wang, *Graduate Student Member IEEE*, Fangxing Li, *Fellow IEEE*, Kevin L. Tomsovic, *Fellow IEEE*, and Joe H. Chow, *Life Fellow IEEE*

ABSTRACT | High penetration of converter-interfaced renewable energy resources will significantly change the swing dynamics between synchronous generators (SGs) in future power systems. This article examines the impact of high converter penetration on wave-like disturbance propagation arising from sudden generator and load losses in radial (1-D) and meshed (2-D) power systems. To keep the uniformity assumption as converters are introduced, the rating of each SG is decreased with a converter resource making up for the reduction. Numerical simulations demonstrate that as the penetration level of constant-power grid-following (GFL) converters increases, the speed of disturbance propagation increases due to the reduced system inertia. Naturally, converters with the capabilities to positively respond to disturbances would in turn reduce the propagation speed. Analytical studies based on continuum models are presented for the 2-D system with SGs and constant-power GFL converters in order to visualize the disturbance propagation and validate numerical simulations based on differential-algebraic equations. In addition, fast active power control of converters can slow down the electromechanical wave (EMW) propagation and even contain it. These concepts are illustrated on the idealized radial and meshed systems and a reduced model of the U.S. eastern interconnection.

KEYWORDS | Converters; electromechanical wave (EMW) propagation; renewable energy resources; U.S. eastern interconnection (EI).

I. INTRODUCTION

Disturbance propagation [1], [2] arising from sudden generator and load losses typically precedes electromechanical swing between generators in a large power system [4]. The seminal work in [1] leads to a large body of additional investigations, such as [2], [5]–[8], where the term "electromechanical wave (EMW) propagation" has been adopted [3], [5], [8], [10], [11] to describe such wave-like propagation of electromechanical motions in generators across the system following a disturbance. With the availability of high sampling rate data from phasor measurement units (PMUs) [9], EMW propagation can be observed and measured, providing opportunities to verify the results mentioned in [1] for real systems and allowing further exploration and understanding of power system dynamics. It also enables application development such as locating disturbance sources [10] and optimal setting of protective relays [11].

Manuscript received 26 November 2021; revised 6 March 2022, 17 April 2022, and 3 May 2022; accepted 3 May 2022. Date of publication 18 May 2022; date of current version 13 July 2023. This work was supported in part by the Engineering Research Center Program of the National Science Foundation, in part by the Department of Energy under NSF Award EEC-1041877, and in part by the CURENT Industry Partnership Program. *(Corresponding author: Joe H. Chow.)*

Hantao Cui is with the School of Electrical and Computer Engineering, Oklahoma State University, Stillwater, OK 74078 USA (e-mail: h.cui@okstate.edu).

Stavros Konstantinopoulos was with the Department of Electrical, Computer, and Systems Engineering, Rensselaer Polytechnic Institute, Troy, NY 12180 USA. He is now with the Electric Power Research Institute, Palo Alto, CA 94304 USA (e-mail: skonstantinopoulos@epri.com).

Denis Osipov and **Joe H. Chow** are with the Department of Electrical, Computer, and Systems Engineering, Rensselaer Polytechnic Institute, Troy, NY 12180 USA (e-mail: osipod@rpi.edu; chowj@rpi.edu).

Jinning Wang, **Fangxing Li**, and **Kevin L. Tomsovic** are with the Department of Electrical Engineering and Computer Science, The University of Tennessee, Knoxville, TN 37996 USA (e-mail: jwang175@vols.utk.edu; fli6@utk.edu; tomsovic@utk.edu).

Digital Object Identifier 10.1109/JPROC.2022.3173813

The study of EMW propagation has been proposed for 1-D radial systems and 2-D meshed systems. A homogeneous 1-D radial power system can be modeled in the limit as a continuum model represented by a partial differential equation (PDE), also known as the wave equation, from which the EMW propagation speed can be derived [1]. Extension to the radial structure includes the modeling of a longitudinal East Australia system [6] and ring systems [2], [3]. Analysis of 2-D power systems using the continuum model is more difficult, depending on the specific structure of the meshed system. In [8], a uniform 2-D square power grid is used to demonstrate the EMW propagation without the constant voltage assumption. A New England power system model is studied in [5] and a four-area Australian system is investigated in [6]. Li *et al.* [7], [8] also developed the use of static var compensator (SVC) control system to mitigate EMW propagation. Sahyoun *et al.* [8] also proposed the use of distributed voltage and power control to reduce the EMW disturbance.

This article investigates the impact of high penetration of converter-interfaced renewable resources on EMW propagation and its mitigation using fast converter active power control. Any inertia of a renewable resource behind a converter is isolated from the ac power grid, leading to the low-inertia phenomenon of future power systems with high renewable penetration. As shown in this article, given a generator-trip disturbance, a system with low inertia sees an increase in both the EMW propagation speed and the depth of the frequency nadir. A faster wave propagation has advantages, such as eliciting faster governor response, but also disadvantages, such as premature load shedding or unintended operation of relays [12]. Thus, a proper understanding of such tradeoff is important, especially for systems with high levels of converter-interfaced renewables. To remedy this situation, various converter control functions have been proposed, such as emulating a conventional synchronous generator (SG). A more advanced approach is the virtual synchronous generator (VSG) concept [16], [18], which will be investigated in Section IV-C.

Increasingly, there is a recognition that converter active power controls can be exercised much faster than SGs [20], including tighter frequency regulation using fast power ramp-up [13] and transient stability enhancement using fast power reduction [15]. While converter-based resources may not be able to sustain additional power outputs for long periods due to active power resource availability, they can be utilized for controlling EMW propagation, which is in the time frame of the first swing (a few seconds). In this article, fast converter control is designed not only to slow down the EMW propagation but also to contain it. Fast converter power control can be more effective than SVC [6], [7], which only regulates the effective series reactance connecting the synchronous machines.

The analysis, simulation, and control designs are performed using a 1-D radial power system and a square 2-D meshed power system. To keep the homogeneity assumption in these systems as converters are introduced, the rating of each SG is decreased with a converter resource making up the reduction. Recognizing that accurate wave equations considering actively controlled inverters are difficult to formulate, we derive and solve the analytical equations for 2-D systems with SGs and constant-power grid-following (GFL) converters using PDEs, that is, the wave equation analysis concerns the dynamics of synchronous machines and does not account for the dynamics of inverters with inertial or primary frequency response capabilities. Nonetheless, disturbances propagate in a wave-like manner, and the analysis of the remaining synchronous machines alone can provide insights into the impact of inverters on wave characteristics. Next, the impact of converters on the EMW propagation speed is studied numerically by simulating differential-algebraic equation (DAE)-based dynamics. Furthermore, the EMW propagation in the 2-D system is compared with that in a reduced model of the U.S. eastern interconnection (EI).

The contributions of the article include: 1) the method of modeling high renewable penetration in a 1-D system for EMW propagation investigations; 2) extension of the analytical EMW speed result in [1] to systems with constant-power GFL converters; 3) numerical studies of the impact of VSG models on EMW propagation in 1-D systems; 4) analytical studies of EMW propagation in 2-D systems with constant-power GFL converters; and 5) converter control design to slow down and contain EMW propagation in 1-D and 2-D systems.

The remainder of this article is organized as follows. Section II describes converter models for renewable energy resources. Section III shows the 1-D system model, and Section IV contains the 1-D system simulation results with converters and the impact of VSG models. Section V presents the converter control design to mitigate a generator loss event, thus slowing down the EMW speed and the spread of the disturbance. Section VI shows the 2-D system model, the EMW PDE formulation, and the analytical solution. Section VII contains the 2-D system simulation results. Section VIII shows the result of applying the converter control to mitigate EMW propagation in the 2-D system. The Appendix shows the derivation and solution of the 2-D EMW equations, along with parameters used in the 2-D square system to approximate the EI system.

II. CONVERTER MODELS FOR RENEWABLE ENERGY INTEGRATION

This section describes the converter models used in this article. Fig. 1 shows the converter model connected to the ac network with an active power supply on the dc side. The power supply can be either a wind turbine, a solar PV system, or a battery system [13], and a control system can be implemented on the converter [14]. Fig. 2 shows the main function blocks of the converter control system, where the controllers are categorized into "reference generators" and

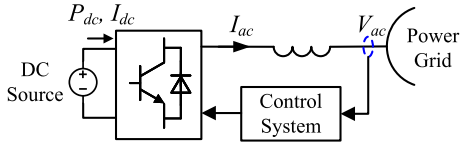

Fig. 1. *Schematic of a grid-connected converter model.*

"reference trackers." Reference generators calculate the power, voltage, or speed references based on the external network and internal device measurements [17]. Reference trackers are subdivided into the electrical controls as the outer loops and the converter interface as the inner loops [12]. In models without reference generators, the references remain constant at the steady-state values.

For renewable energy integration, the converter interfaces can be controlled in the GFL or the grid-forming (GFM) mode [14]. GFL converters, shown in Fig. 3, accept active and reactive power references (P_{ref} and Q_{ref}) from external controllers to compute the internal current references based on measured network voltages. Notably, GFL converters utilize phase-locked loops (PLLs) to synchronize with the grid [12], [32]. GFM converters, shown in Fig. 4, accept voltage and angular frequency references (V_{ref} and ω_{ref}) to compute internal angle and voltage references before computing the current references [16]. GFM converters synchronize with the grid based on the internal reference speed ω_{ref}, which can be generated by droop and/or VSG control [26].

GFL converters can be linked with external controllers to respond to voltage and frequency deviations, as shown in Fig. 28 in Appendix D. The voltage control loop modifies the reactive power reference Q_{ref} typically using a proportional-integral (PI) controller based on voltage deviation. Also, the frequency control loop modifies the active power reference P_{ref} using a proportional-derivative (PD) controller based on frequency deviation, the derivative of which is the rate-of-change of frequency (RoCoF). These controllers will impact the EMW propagation by affecting

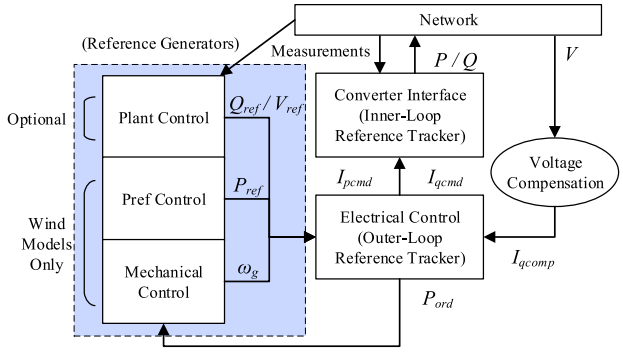

Fig. 2. *Overview of the control systems of grid-connected converters.*

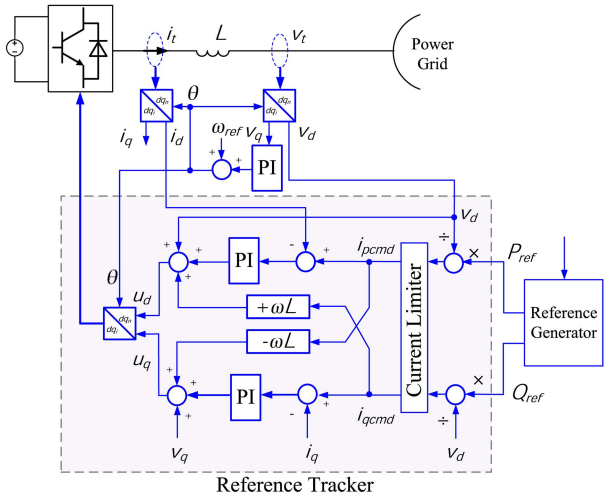

Fig. 3. *GFL converter: inner loop and outer loop diagrams.*

voltages and active power outputs. Their effects will be quantified by simulation in Sections III–V.

The inner current control loop of both GFL and GFM converters is used for representing the average output of the switching power electronics. For system-level stability studies, the inner loop PI controllers can be simplified with a first-order delay for the current, followed by algebraic equations that link the converter terminal voltage u with the grid voltage v [21]. For example, Fig. 5 shows the GFM converter based on such simplification.

III. HOMOGENEOUS 1-D RADIAL SYSTEM

Consider the uniform 1-D system of $N+1$ buses and N transmission lines shown in Fig. 6 [22]. Each bus has one generator attached, and generators G_1 to G_N are identical in MVA rating S_n and inertia H. The classical generator model consisting of one generator angle state and one generator speed state is used throughout this

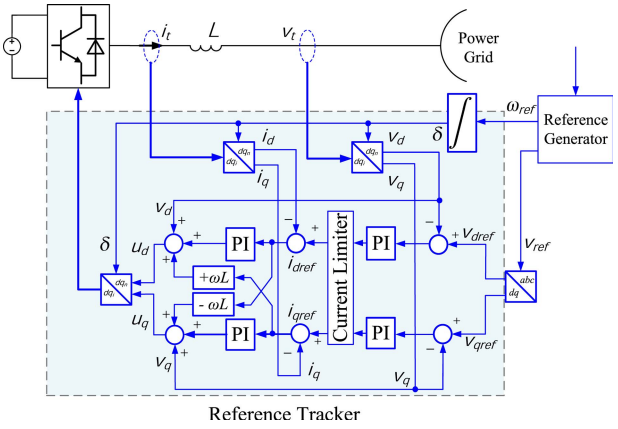

Fig. 4. *GFM converter: inner loop and outer loop diagrams.*

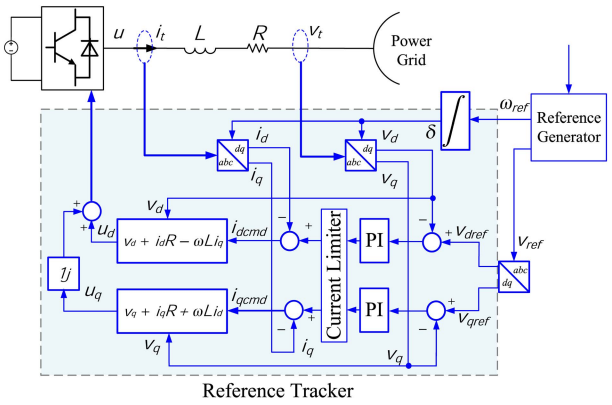

Fig. 5. *GFM converter with simplified inner loops.*

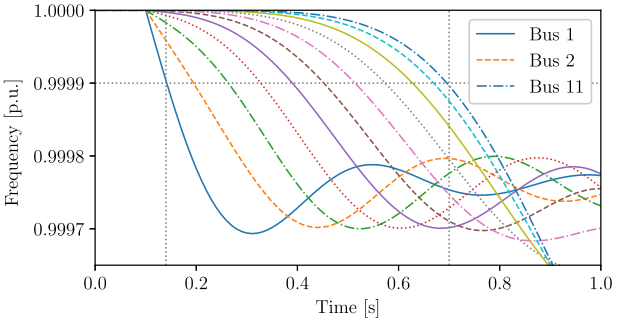

Fig. 7. *Base case EMW propagation showing frequencies at all buses.*

article unless mentioned otherwise. Generator G_0 can use arbitrary parameters as will be disconnected to create a disturbance. Active power P_e is supplied from G_0 and G_1 to G_N, which acts as a load. Each of the other generators (G_2–G_{N-1}) supplies its local load such that the power flow from Bus 1 to Bus N through each line with reactance X is also P_e. Converters are added in parallel with G_2–G_{N-1}, which do not inject active power to the grid at the steady state.

To study the impact of the converters while preserving the homogeneity from Bus 2 to Bus $N-1$, the ratings of the generators G_2–G_{N-1} will each be reduced to $(1-\rho)S_n$ and a converter with rating of ρS_n will be installed on the same generator bus, where $0 \le \rho \le 1$ is the ratio of renewable/converter penetration, as shown in Fig. 6. To preserve at least one swing mode in the system, generators G_1 and G_N are kept at their original ratings.

The disturbance considered is the trip of generator G_0 by opening the circuit breaker (CB) that connects Bus 0 to Bus 1. This disturbance will result in a frequency drop propagating from G_1 to G_N. Note that such disturbances may not always provoke steam governor response, as is the case observed in the U.S. EI [33]. If the renewables are interfaced by GFL converters that are not configured to respond to frequency drops, the EMW propagation speed c then requires inserting a factor $(1-\rho)$ in the formula in [1] to account for the inertia reduction, effectively increasing the propagation speed, given by

$$c = \sqrt{\frac{\Omega}{2(1-\rho)hx}} \text{ pu-length/s} \tag{1}$$

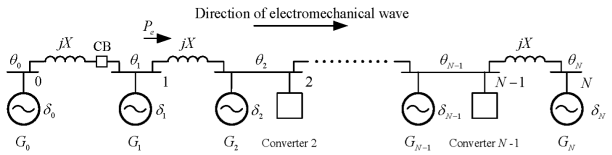

Fig. 6. *1-D radial power system.*

where $\Omega = 2\pi f_n$, $h = dH/d\ell$, $x = dX/d\ell$, and f_n is the nominal frequency in hertz. All quantities need to be converted to the same power base, and the base for distance is the total length of transmission lines in the postfault system. Note that (1) is derived from the continuum model of the 1-D system for describing the speed of the forward and backward waves. In actual systems, wave reflections will introduce slight errors in the measurement of EMW propagation speed toward generator G_N, as will be discussed in Section IV.

IV. 1-D SYSTEM ANALYSIS

A. Base Case

In the base case ($\rho = 0$) with $N = 11$, each SG is rated at $S_n = 200$ MVA, $H = 3$ s, and damping coefficient $D = 1$ pu in the machine base. Each reactance connecting the generators is $X = 0.1$ pu in the 100-MVA base. The initial outputs of G_0, G_1, and G_{11} are 5, 145, and -150 MW, respectively. The introduced disturbance at $t = 0.1$ s is the CB opening event, which will cause sequential frequency drops on all buses.

To compute the theoretical EMW propagation speed, let the length between Buses 1 and N be 1 pu-length. In 100-MVA base, the system with 11 generators and 10 lines has

$$\begin{aligned} x &= 0.1 \times 10/1 = 1 \text{ pu-reactance/pu-length} \\ h &= 2 \times (3 \times 11)/1 = 60 \text{ s/pu-length}. \end{aligned} \tag{2}$$

Substituting h and x into (1) yields $c = 1.690$ pu-length/s. Thus, the predicted EMW propagation time from Bus 1 to Bus 11 is $1/c = 0.592$ s.

We note that the EMW propagation time between two buses is measured as the time difference for the bus frequencies to drop to a chosen threshold. In this case, the threshold is chosen as 0.9999 pu (59.994 Hz).[1] As shown in Fig. 7, the disturbance takes 0.04 and 0.6 s to reach

[1]The threshold is chosen based on the amount of generation or load tripped and the total system inertia. It thus varies with the disturbance and the system model.

Table 1 Speed Based on (1) and Arrival Times From (1) and Simulation

		$\rho = 0$	$\rho = 0.25$	$\rho = 0.5$	$\rho = 0.75$
c from (1) in per unit X/s		1.772	2.047	2.507	3.545
Arrival Time in s	from (1)	0.564	0.489	0.399	0.282
	from simulation	0.560	0.462	0.363	0.280

Buses 1 and 11, respectively. Hence, the EMW propagation time is 0.560 s, which is close to 0.592 s as predicted by (1).

For the last few buses, the frequency drop is more rapid than the first several buses because, by the time the disturbance propagates to the other end, the frequency of the first few buses has partially recovered from the nadir, causing larger power mismatches and thus larger deceleration at the terminal generators. The larger deceleration causes the terminal buses to reach the threshold more quickly. A similar phenomenon can be observed in the 2-D system discussed in Section VI and its visualization in Fig. 19.

B. Systems With Converter-Interfaced Renewable Generators

Radial systems with converter-interfaced renewable generators (RGs) are created with $\rho = 0.25$, 0.5, and 0.75. The models employed are the second-generation generic models [17], which are fundamentally GFL converters. Such models have the capability to regulate the bus voltage by a PI controller. We also extend the GFL converter models to emulate inertial response using a derivative control based on the local frequency. Note that for GFL and GFM converters providing grid support and control functions, models with much more details would be required to study wave propagation at the interfaces between the converters and the ac power grid in terms of dispersion and reflection. The aim of this article is to examine converter control actions at a higher level using the DAE simulation. This section will investigate how voltage control and inertia emulation by renewables affect the EMW propagation.

1) Impact of Voltage Control: First, the GFL converters are controlled to constant Q_{ref}, namely, without voltage control, and simulated for the same disturbance. The propagation speeds and arrival times are shown in Table 1, in which the analytical results from (1) are supported by simulation results with errors less than 10%.

Then, GFL converters are applied to control reactive power setpoint to regulate the bus voltage. Systems examined in this article have typical line reactances to support sufficient amount of power transfer. The control parameters for the converters are $V_{\text{REF}} = 1.0$ pu, $K_{vp} = 0.5$, and $K_{vi} = 0$, where V_{REF} is the voltage setpoint and K_{vp} and K_{vi} are the proportional and integral control gains, respectively. Fig. 8 shows the results of the three voltage-controlled RG scenarios. As observed, the impact of voltage control on the EMW propagation speed is limited and can be neglected.

2) Impact of Inertia Emulation: A converter control that can impact the EMW propagation speed is to modify the active power reference based on the RoCoF [25]. Known as inertia emulation, such a derivative control provides additional active power support to emulate the inertial response natural to SGs. The additional power ΔP_{IE} that adds to P_{ref} in Fig. 3 is calculated from the following:

$$\Delta P_{\text{IE}} = K_{\text{df}} \times \text{RoCoF} \tag{3}$$

where K_{df} is the frequency derivative control gain and RoCoF is measured locally. K_{df} has the same dimension as inertia. Still, the impact of K_{df} from GFL converters is determined by both the power and current control loops, which are subject to delays and nonlinearities such as limiters. Thus, the impacts on the EMW propagation speed have to be shown by simulation.

Fig. 9 compares the frequency at Bus 11 for $\rho = 0.25$, 0.5, and 0.75 with different gains. The vertical dashed lines correspond to the arrival time at Bus 11 for $\rho = 0$. Overall, inertia emulation control can significantly slow down the EMW propagation. A higher gain can be more effective in slowing down the EMW propagation at the expense of more active power headroom on the dc side. Also, it can be observed that the gain K_{df} to restore to the original propagation time increases from below 20 for the 25% case to above 20 for the 50% and 75% cases.

C. Virtual Synchronous Generators

An alternate means of providing inertial response is to emulate SGs using GFM converters. Following a disturbance, the deviation of the converter power output can be utilized for calculating the speed reference based on the

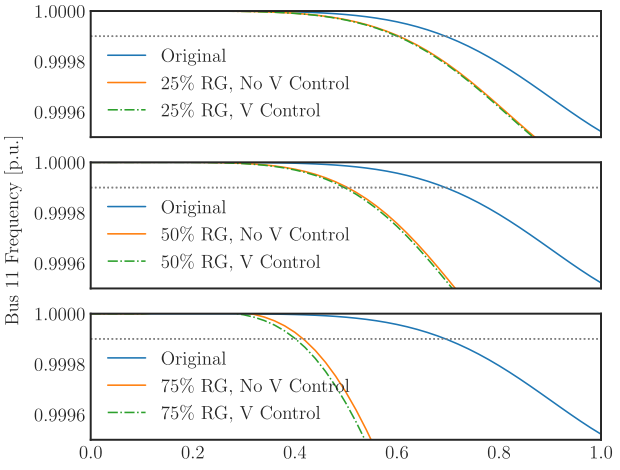

Fig. 8. ***Frequency at Bus 11 with and without voltage control.***

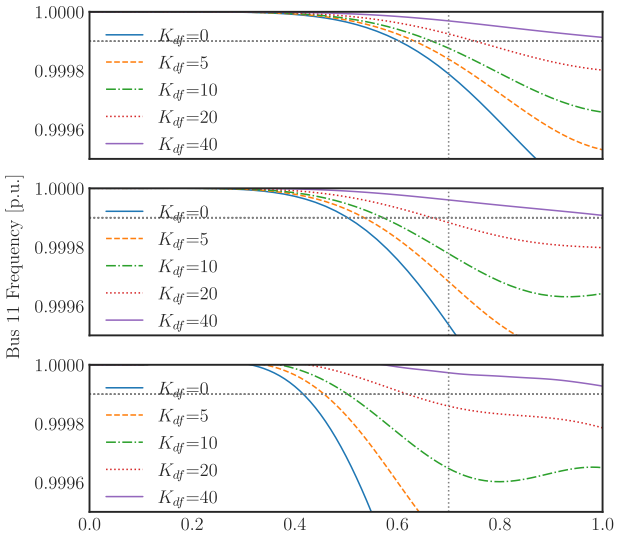

Fig. 9. *Bus 11 frequency with inertia emulation from converters—top: 25% RG, middle: 50% RG, and bottom: 75% RG.*

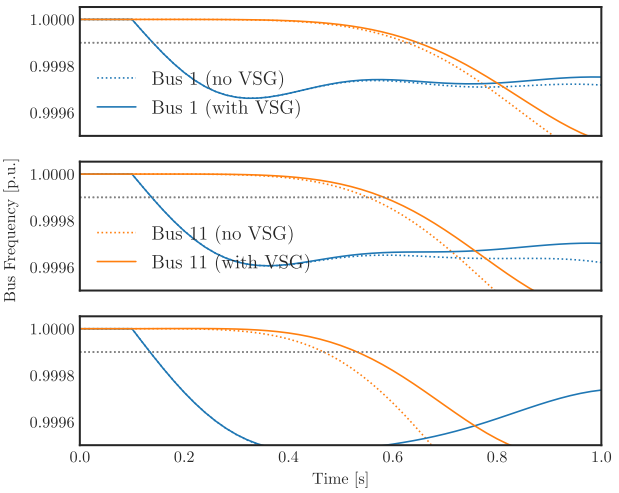

Fig. 10. *Bus frequency with and without VSG. From top to bottom: $\rho = 0.25$, 0.5, and 0.75.*

swing equation

$$2H_{\text{VSG}}\dot{\omega}_{\text{VSG}} = P_{\text{set}} - P_e - D(\omega_{\text{VSG}} - 1) \tag{4}$$

where ω_{VSG} is the per-unit speed of the converter internal reference frame, H_{VSG} is the emulated inertia in seconds, P_{set} is the per-unit active power setpoint, P_e is the per-unit converter active power output, and D is the emulated damping coefficient in per unit. The variable ω_{VSG} integrated from (4) is used as the speed reference ω_{ref} in Figs. 4 and 5, and the corresponding control loop to generate ω_{VSG} is shown in Fig. 29 in Appendix D. GFM converters with such inertial response capability are referred to as VSGs [26]. This section investigates how VSG parameters influence the EMW propagation speed using the simplified GFM converter model in Fig. 5.

Two parameters in the VSG model can affect the EMW propagation speed: the emulated inertia H_{VSG} and the outer loop voltage control gain K_p, which is the proportional gain for the PI controllers shown in Fig. 5. Initially, the amount of reduced SG inertia is compensated exactly by a VSG with the same inertia and a small gain $K_p = 0.3$. Fig. 10 shows the EMW propagation from Bus 1 to Bus 11 for systems with $\rho = 0.25$, 0.5, and 0.75. Further investigation shown in Fig. 11 shows that further increasing the inertia H_{VSG} only has minor impact on the EMW propagation speed, and a small value for H_{VSG} is common for VSG [12]. On the other hand, the investigation shows that the voltage control gain has a significant impact on reducing the EMW propagation speed.

The impact of the voltage control gain K_p is analyzed using the system with $\rho = 0.5$ as an example. Fig. 12 shows the frequency at Bus 11 for $K_p = 0.3$, 0.65, and 1.0, and the corresponding arrival times are 0.585, 0.638, and 0.707 s, respectively. It is observed that increasing K_p will slow down the EMW propagation. With $K_p = 1.0$, the EMW propagation speed is slightly lower than that of the fully synchronous system. Also, the active power output patterns of SGs and VSGs on Buses 2–10 are shown in Fig. 13, where inertial response of VSGs is observed but more limited in magnitude compared with SGs. This power output difference is that the SG output is a natural response to the change of network flow through stator/rotor electromagnetic fluxes, whereas the VSG output is a controlled response.

V. EMW MITIGATION

Converters with energy supply have the capability to inject additional active power into the network at a fast time scale. Such a capability can potentially be used to mitigate EMW propagation, which is discussed in this section. In contrast, the active power maneuvering of steam and hydraulic turbines is much slower and thus cannot be used for this purpose. Control algorithms presented next will be applied to Type-3 wind turbines but is also applicable to Type-4 wind turbines or PV plants.

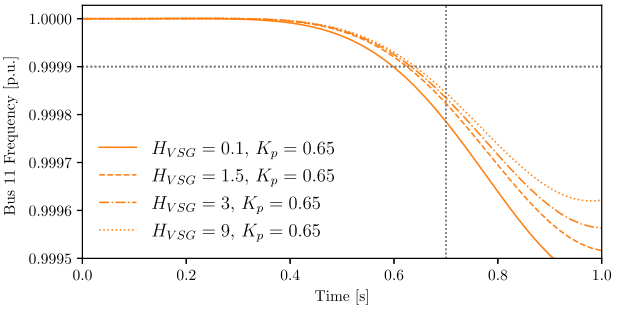

Fig. 11. *Bus frequency for $\rho = 0.5$ with different VSG inertias.*

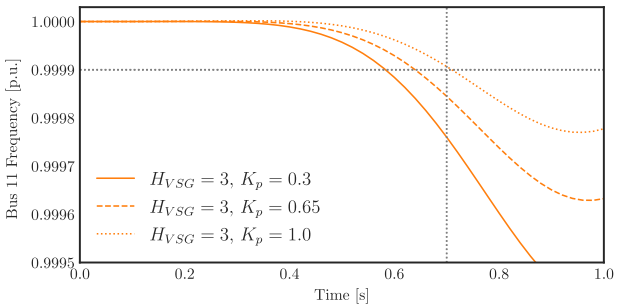

Fig. 12. *Bus frequency for $\rho = 0.5$ with different voltage control gains.*

A. Active Power Flow Control

Consider the active power flow control between the two buses shown in Fig. 14. The injections P_1 and P_2 on Buses 1 and 2, respectively, are controllable. With power flowing from Bus 1 to Bus 2, the active power conservation equations dictate that

$$P_{\text{in}} + P_1 = P_{12} = P_{\text{out}} - P_2. \tag{5}$$

Decompose the individual power flow into a steady-state component, denoted by a bar over the variable, and a perturbation component denoted by the prefix Δ as

$$\begin{aligned} P_{\text{in}} &= \bar{P}_{\text{in}} + \Delta P_{\text{in}},\ P_{12} = \bar{P}_{12} + \Delta P_{12} \\ P_{\text{out}} &= \bar{P}_{\text{out}} + \Delta P_{\text{out}}. \end{aligned} \tag{6}$$

The aim is to introduce an attenuation of the incoming perturbation ΔP_{in} by controlling the two active power

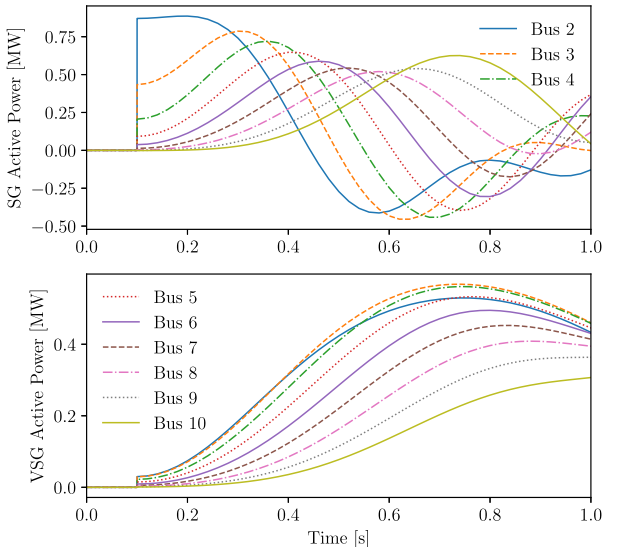

Fig. 13. *SG and VSG power outputs for $\rho = 0.5$ and $H = 3$ s.*

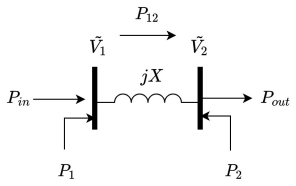

Fig. 14. *Two-bus system with two active power injections.*

injections. Consider the control law

$$P_1 = -K_1 \Delta P_{\text{in}}, \quad P_2 = -K_2 \Delta P_{12},\ 0 \le K_i \le 1. \tag{7}$$

Each injection monitors the upstream line flow perturbation and enacts a proportional control response to counter the flow deviation. Substituting the control law (7) into the active power flow equations (6), assuming that all flows have the same steady-state value, results in

$$P_{\text{out}} = \bar{P}_{\text{in}} + (1 - K_1)(1 - K_2)\Delta P_{\text{in}}. \tag{8}$$

Thus, the perturbation component ΔP_{in} will be attenuated by $(1 - K_1)(1 - K_2)$. In the case of a radial connection of N wind turbine generators (WTGs), the measured perturbation on the line between Buses $N - 1$ and N is

$$\Delta P_{\text{out}} = \left(\prod_{i=1}^{N} (1 - K_i) \right) \Delta P_{\text{in}} \tag{9}$$

which can be small when $K_i, i = 1, \ldots, N$, are close to unity or N is large. In the case of a Type-3 wind turbine [24], the active power injection will be superimposed on the active power command of the plant. The WTG realizes an active power current command as

$$I_{\text{pcmd}} = \frac{P_{\text{set}} - K\Delta P}{V_t}. \tag{10}$$

The command is realized as output current from the converter, with a time constant of 10–20 ms. The power setpoint P_{set} is derived by a torque controller, modulating the speed of the WTG. Nonetheless, these dynamics are slower than the scale we exercise our control to halt the disturbance. For the full active power control dynamics, the reader can refer to [24].

B. Reactive Power Damping Control

Active power injection by the converters will not completely mitigate EMW propagation because the electromechanical oscillations between the synchronous machines will still persist. An expedient means to damp the oscillations is to use reactive power injection.

In a Type-3 wind turbine, active and reactive power can be controlled in a decoupled manner. The reactive power is controlled by the flux of the WTG units. The reactive power control dynamics can be summarized as [24]

$$Q_{\text{ord}} = \frac{1}{T_c s + 1}\left(\frac{K_{pv}}{T_V s + 1} + \frac{K_{iv}}{s}\right)\left(V_{\text{ref}} - \frac{V_{\text{reg}}}{T_r s + 1}\right) \tag{11}$$

$$R_{\text{err}} = \frac{K_{Qi}}{s}(Q_{\text{ord}} - Q) \tag{12}$$

$$E_{\text{fd-cmd}} = \frac{K_{Vi}}{s}(R_{\text{err}} - V) - \frac{K_Q}{s}\Delta P \tag{13}$$

where Q_{ord} is the reactive power command of the plant, R_{err} is the local dynamic voltage reference, and $E_{\text{fd-cmd}}$ is the flux command, which is applied behind an equivalent reactance X. K_{pv} and K_{iv} are the PI gains of the voltage control, T_c is the time constant of the reactive power command dynamics, T_V is the proportional gain filter time constant, T_r is the regulated voltage transducer time constant, K_{Qi} is the gain of the reactive power regulator, and K_{Vi} is the gain of the local voltage regulator. V denotes the local WTG voltage and V_{reg} is the point of which the WTG regulates voltage.

To provide damping to electromechanical swings, one approach is to modulate the reactive power injection using the line power flow perturbation as the input signal. The damping controller, in certain situations and with particular choice of feedback signals, can require a phase lag in the compensator design [23]. The feedback signal can be incorporated into the $E_{\text{fd-cmd}}$ dynamics (the converter time delay is omitted as it is in the range of milliseconds). The integrator provides the necessary lag to modulate the reactive power to introduce damping to the electromechanical swings.

In addition, assuming that the WTG has the headroom to drive ΔP to zero, the damping control term in (13) will not affect steady-state voltage regulation. To demonstrate the efficacy of the design, for the radial system, the response of the first WTG in the chain is plotted in Fig. 15, for the values 0 and 0.2 of K_Q, while the active power control is also exercised. The values for this design were tuned via an iterative process while considering the damping performance of the system and the disturbance propagation speed. Multiple-input–multiple-output techniques can be utilized in more mesh and complex systems.

C. Application to Radial System

To illustrate the performance of the proposed control, the 1-D system in Fig. 6 with 100% converter penetration is investigated. The WTG model in [24] is used to model the converters. Note that the resulting network still has two synchronous machines on Buses 1 and 11. The disturbance is the separation of G_0 from the network at $t = 0$ s. Several values of K_i are used, and the reactive power damping control is tuned to damp the oscillation between G_1 and G_{11}. Without this mitigation control, the EMW propagation

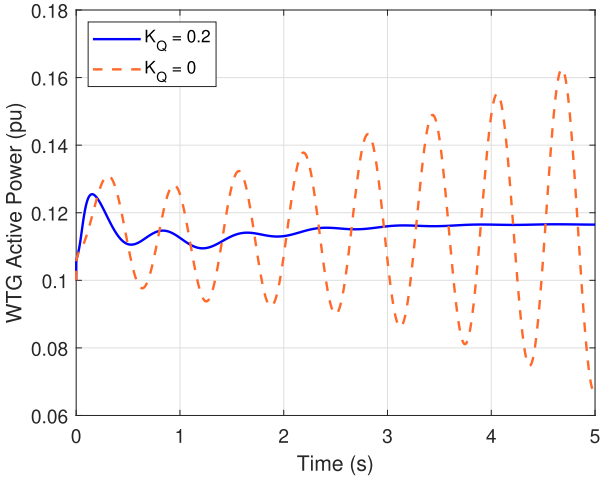

Fig. 15. *WTG2 active power output for different damping control gains.*

time for Bus 11 to reach a frequency of 0.9999 pu drops to 0.199 s, as shown in Fig. 16. When the mitigation control with $K = K_i = 0.4$ is applied to all converters $i = 2, \ldots, 9$, and the damping control K_Q tuned to 0.1, the propagation waves are shown in Fig. 16(b). For $K = 0.4$, the frequency drop does not fall below 0.9999 pu. Thus, the EMW propagation is completely mitigated for buses far from the disturbance source.

For $K = 0.4$, the additional active power injection provided by the converters on Buses 2–10 is shown in Fig. 17. As expected, converters closer to the disturbance provide more active power support. The damping control function also works well with the electromechanical swings subsiding within 3 s.

VI. 2-D MESHED SQUARE SYSTEM

Practical power systems typically cover well-connected geographical regions and thus should be modeled as

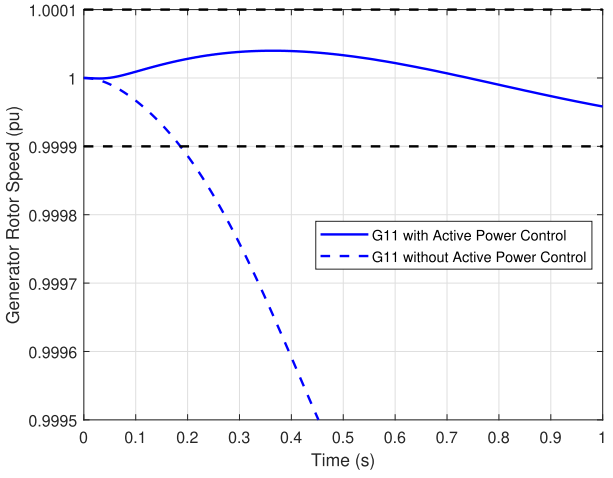

Fig. 16. *Radial system SG speeds $\rho = 100\%$ with and without active power flow control.*

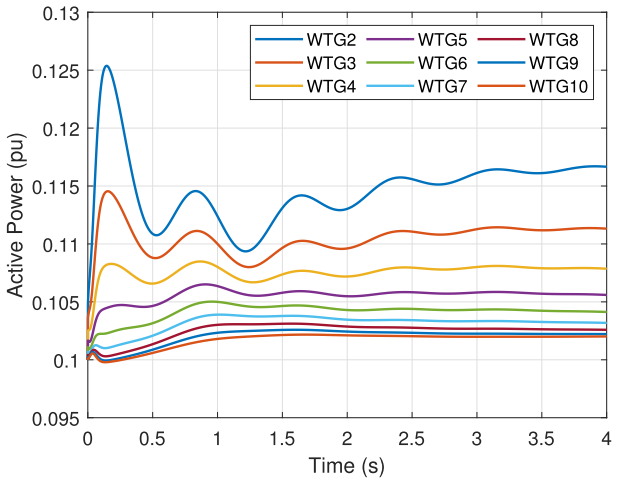

Fig. 17. *WTG active power generation with active power flow control.*

2-D meshed systems. Consider the 10×10 grid system in Fig. 18 representing a uniform 2-D power system. Node (i, j) denotes the bus with generator $G_{i,j}$ with MVA rating S_n and inertia H on the generator base. All the generators and the reactance X (on the MVA base S_n) between each pair of buses are identical. Active power P_e is supplied from $G_{1,1}$ to $G_{10,10}$, which acts as a load. The considered disturbance is the load trip at Node (1,1). This section will establish the continuum model-based PDE to model the EMW propagation, solve the PDE analytically, and compare the EMW propagation pattern with that from the DAE model.

A. Analytical Derivation of 2-D Wave PDE

While it is intriguing to develop analytical PDE formulations for systems with detailed converter models, there are fundamental difficulties in considering inverters with multiple control loops in wave equations. The inclusion of controllers will affect converter power outputs and result in a complex PDE model, which analytically reveals no new information on the propagation characteristics and is numerically extremely challenging to solve. We consider SGs and constant-power-controlled GFL converters when deriving the EMW equation for a 2-D meshed power system using the continuum and dc power flow assumptions. The full derivation is shown in Appendix A following the same PDE for a rectangular membrane wave problem [28]. Here, the temporal and spatial variations of the rotor angle δ in the 2-D meshed power system continuum model are

$$\ddot{\delta} = c^2 \left(\delta_{xx} + \delta_{yy}\right) \tag{14}$$

where $\ddot{\delta}$ is the second-order time derivative of δ, δ_{xx} and δ_{yy} are the second-order spatial derivatives in the horizontal and vertical directions, and c is a constant that, for a square system, shares the same formula as in (1). Note that c, such as in the 1-D system, has the dimension of pu-length/s. Analytical solutions to (14) at the end of this section will verify that c is the propagation speed.

To solve for $\delta(x, y, t)$, techniques such as separation of variables can be applied, followed by the application of the initial conditions and boundary conditions. The resulting solution

$$\delta(x, y, t) = H(x)Q(y)G(t) \tag{15}$$

where $H(x)$, $Q(y)$, and $G(t)$ are the separated functions as derived in Appendix B. Here, we show the development of the chosen initial and boundary conditions for a square grid model. Since the EMW propagation of interest is in the time frame of the first swing, the propagation will be best observed if the system starts in a steady state before the disturbance is applied. The disturbance chosen happens at just one corner of the system.[2] Therefore, the initial conditions are chosen as

$$\begin{aligned} \delta(x, y, 0) &= 0 \\ \dot{\delta}(x, y, 0) &= \begin{cases} \Omega \times \Delta\omega_0, & \text{if } x = y = 0 \\ 0, & \text{otherwise} \end{cases} \end{aligned} \tag{16}$$

where (x, y) are the coordinates in the continuum model and $\Delta\omega_0$ is the initial speed deviation at the source $(0, 0)$. This disturbance can be considered as an impulse as speed at the disturbance initiation point is changed instantaneously.

The boundary conditions constrain the motion of the generators on the four edges over time. We observe that the sensitivity of rotor angles on the boundary to infinitesimal spatial variation along the direction is zero. In other words, when the wave traveling along the x-axis reaches the end, the spatial variation with respect to the

[2]This is motivated by a disturbance initiated in Florida of the U.S. eastern power grid in 2008.

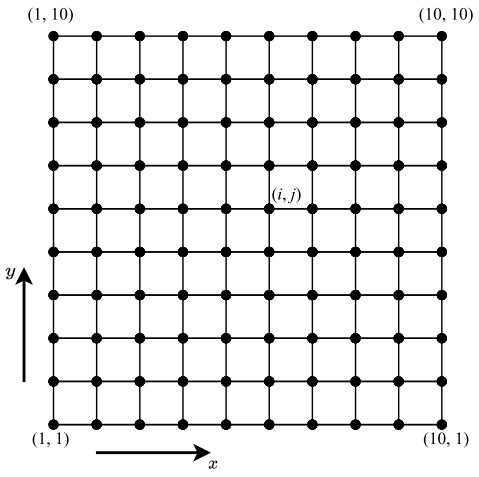

Fig. 18. *2-D meshed power system.*

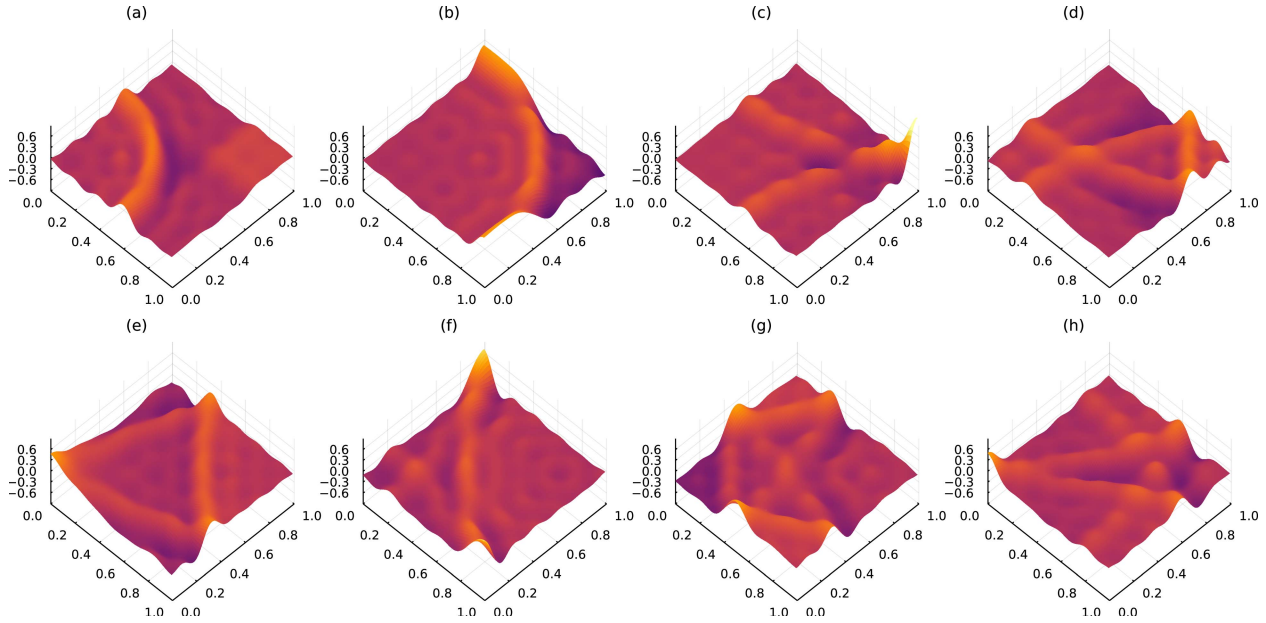

Fig. 19. *EMW propagation in the 2-D system based on PDE. (a) and (b) Forward EMW propagation to the edges ($t = 0.33$ s and $t = 0.56$ s, respectively). (c) and (d) Continuing propagation to the diagonal node and the subsequent reflections ($t = 0.77$ s and $t = 0.90$ s, respectively). (e)–(h) Superposition of reflection waves ($t = 1.05$ s, $t = 1.20$ s, $t = 1.35$ s, and $t = 1.51$ s, respectively).*

displacement along the x-axis can only become zero. Thus, the wave has to travel in the perpendicular direction. Therefore, the boundary conditions are given by

$$\begin{aligned} 0 &= \left.\frac{\partial \delta}{\partial x}\right|_{0,y} = H_x(0)Q(y)G(t) \\ 0 &= \left.\frac{\partial \delta}{\partial x}\right|_{0,a} = H_x(a)Q(y)G(t) \\ 0 &= \left.\frac{\partial \delta}{\partial y}\right|_{x,0} = H(x)Q_y(0)G(t) \\ 0 &= \left.\frac{\partial \delta}{\partial y}\right|_{x,b} = H(x)Q_y(b)G(t) \end{aligned} \tag{17}$$

where a and b are the length of the grid in the x-axis and y-axis, respectively.

The final solution to the 2-D EMW wave equation is a double series summation with indices $m, n \in \mathbb{N}$, which is given by

$$\delta(x,y,t) = \sum_{m=1}^{\infty}\sum_{n=1}^{\infty} B'_{m,n} \times \cos\left(\frac{m\pi}{a}x\right)\cos\left(\frac{n\pi}{b}y\right)\sin(\lambda_{m,n}t) \tag{18}$$

where

$$\lambda_{m,n} = c\pi\left[\left(\frac{n}{b}\right)^2 + \left(\frac{m}{a}\right)^2\right]^{1/2} \tag{19}$$

$$B'_{m,n} = \frac{4}{ab\lambda_{m,n}}\int_0^b\int_0^a f(x,y)\cos\left(\frac{m\pi}{a}x\right) \times \cos\left(\frac{n\pi}{b}y\right)dxdy. \tag{20}$$

In a square grid, one can use $a = b = L$. Note that $\lambda_{m,n}$ are the eigenvalues of the PDE. As the orders of m and n increase, the amplitude $B'_{m,n}$ will decrease.

B. Approximate Solution to the 2-D Wave PDE

The solution of the PDE can be approximated with sufficiently high orders. First, the propagation speed c is calculated. Suppose that each edge of the 2-D grid has a length of $a = b = 1$ pu. Next, we apply the same parameters of generators and transmission lines to the system with ten generators and nine lines on each edge, namely, each generator has $H = 6$ s, and each line has $X = 0.1$ pu. Thus, c is given by

$$c = \sqrt{\frac{\Omega}{2mx}} = \sqrt{\frac{2\pi f}{2 \times 60 \times 0.9}} = 1.868 \text{ pu-length/s}. \tag{21}$$

Substitute c into (18) and evaluate the expression for $m = 1, 2, \ldots, 10$ and $n = 1, 2, \ldots, 10$, and we can obtain a high-order solution with sufficient accuracy. The spatial solution is discretized in a grid with $\Delta x = \Delta y = 0.01$. Fig. 19 visualizes the EMW wave in the initial propagation from (0, 0) and the subsequent reflections. In Fig. 19(a), one can clearly see the wavefront as it propagates in a quarter circle. Fig. 19(b) shows that the other edges in the x-axis and the y-axis reach the largest magnitude at $t = 0.5601$ s. While the EMW continues to move toward the diagonal, waves reflect at the two boundaries opposite to the source of the disturbance, as shown in Fig. 19(c).

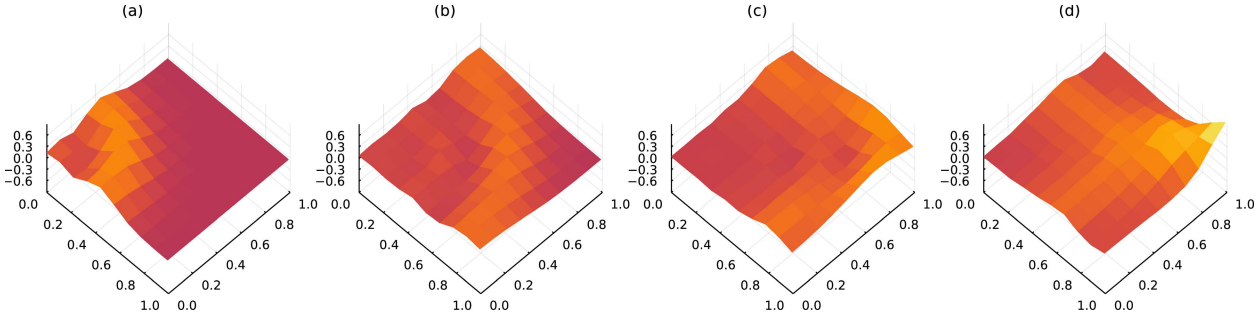

Fig. 20. *EMW propagation in the 10 × 10 2-D meshed power system based on DAE. (a) $t = 0.33$ s. (b) $t = 0.56$ s. (c) $t = 0.77$ s. (d) $t = 0.90$ s.*

After reaching the diagonal, the EMW also reflects in a quarter-circle shape, as shown in Fig. 19(d)–(f). It is also observed that the magnitude of the wave is larger in Fig. 19(b) than Fig. 19(a) and even larger in Fig. 19(c) due to the geometry of the square system and that the disturbance starts at a corner. The remaining subfigures show the superposition of multiple reflection waves. Also, the theoretical propagation time to the opposite nodes, i.e., (0, 1) and (1, 1), is given by $t = 1/c = 0.535$ s, which is verified in Fig. 19(b).

C. Comparison of the PDE and DAE Solutions

To validate the PDE-based method for modeling 2-D wave propagation in power systems, the meshed power system shown in Fig. 18 is simulated using a power system simulator as a comparison. The following settings are used to create the same system configuration and initial conditions.

1) Since the generator transient reactance X'_d is not modeled in the PDE, all generators have $X'_d = 10^{-4}$ pu to minimize its impacts.
2) All generators are initialized at zero power output so that the initial rotor angles $\delta_{i,j}$ are uniformly zero.
3) After the initialization of the disturbance, the speed on the generator at $(1, 1)$ is increased to $\omega_{(1,1)} = 1.08$ pu as a disturbance.

The simulation based on DAE is performed in ANDES [29] and visualized in Fig. 20, and the timestamps shown are the same as in Fig. 19(a)–(d). The EMW propagation can be clearly seen in Fig. 20 by observing the wavefront shown in lighter colors. Comparing the DAE solution with the PDE one, one can observe the similarity in the pattern of EMW propagation. For example, the wavefront arrival at the end of the x- and y-axes is observed in Figs. 19(b) and 20(b), so are the reflection waves in Figs. 19(d) and 20(d). Also, due to discretization, the waveform from the DAE solution appears less pronounced and more diffused, resembling a coarse-grained solution of the PDE in a multigrid method. Nevertheless, the comparison clearly demonstrates the effectiveness of the PDE-based continuum model for EMW propagation study in 2-D power systems.

VII. 2-D SYSTEM SIMULATION RESULTS

While a continuum PDE model can be used to emulate a power system with generators represented as classical models and converters modeled as constant-power injections, in which any inertia behind the converters is not visible from the grid, EMW propagation in 2-D systems with full models of converters needs to be investigated using DAE-based simulations. For the square system considered here, the boundary nodes from (1, 1) to (1, 10) and from (1, 1) to (10, 1) form a horizontal-direction radial system and a vertical-direction radial system, respectively, allowing the use of 1-D system arrival time computation. For the interior nodes and the boundary nodes from (2, 10) to (10, 10) and from (10, 2) to (10, 10), they all have two incoming EMWs such that the 1-D system analysis does not apply. Hence, the behavior of this 2-D system with and without converters will be investigated by simulation.

To study the impact of converters while keeping the uniformity throughout the 2-D system, the ratings of the generators, except for $G_{1,1}$ and $G_{10,10}$, will each be reduced to $(1 - \rho)S_n$ and a converter with rating of ρS_n is installed on the same generator bus, where $0 \leq \rho \leq 1$ is again the percent of converter penetration (see Fig. 21). The disturbance considered is the trip of a load ΔP_e on Bus (1, 1). At a result, the excess generation on Bus (1, 1) will propagate as a rising frequency wave toward Bus (10, 10).

A. Base Case

The 2-D system uses the same generator and reactance parameters of the 1-D system. The simulated propagation time of the base case for the threshold of 60.03 Hz is listed in Table 2. Due to the system symmetry, the propagation time is symmetric with respect to the main diagonal. With $X = 0.1$ pu and $H = 6$ s on 100-MVA base, the propagation speed is with $c = 1.868$ pu-length/s as given in (21), and the predicted time from Node (1,1) to Node (1,10) is thus 0.535 s. The prediction differs from the simulated propagation time of 0.532 s by 0.5%.

As expected, Table 2 shows that the propagation times in the internal nodes are not uniform. An important observation is that the internal nodes have shorter arrival time. For

Table 2 Time to Reach the Frequency Threshold for Buses in the 2-D System

	1	2	3	4	5	6	7	8	9	10
1	0.109	0.148	0.213	0.281	0.349	0.419	0.489	0.556	0.612	0.641
2	0.148	0.191	0.243	0.302	0.366	0.432	0.499	0.565	0.619	0.647
3	0.213	0.243	0.286	0.338	0.395	0.456	0.519	0.582	0.634	0.660
4	0.281	0.302	0.338	0.383	0.433	0.489	0.548	0.607	0.654	0.679
5	0.349	0.366	0.395	0.433	0.479	0.529	0.584	0.638	0.681	0.703
6	0.419	0.432	0.456	0.489	0.529	0.575	0.625	0.674	0.712	0.731
7	0.489	0.499	0.519	0.548	0.584	0.625	0.670	0.713	0.745	0.762
8	0.556	0.565	0.582	0.607	0.638	0.674	0.713	0.750	0.778	0.792
9	0.612	0.619	0.634	0.654	0.681	0.712	0.745	0.778	0.804	0.817
10	0.641	0.647	0.660	0.679	0.703	0.731	0.762	0.792	0.817	0.831

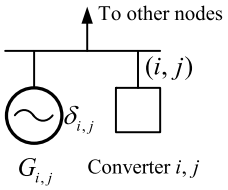

Fig. 21. ***Converter model for 2-D system.***

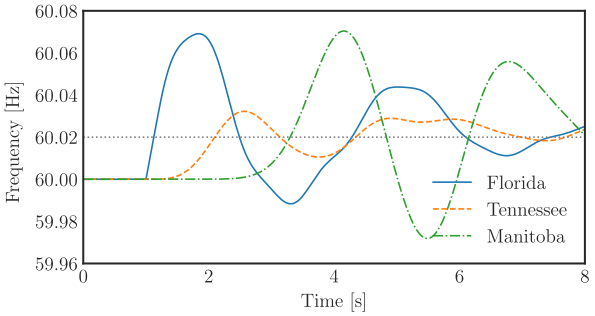

Fig. 22. ***EMW propagation of the simulated Florida event across EI.***

example, the travel time from Node (1, 1) to Node (1, 3) is 0.104 s, whereas that of Node (1, 1) to Node (2, 2) is 0.082 s, even though Nodes (1, 3) and (2, 2) are both two branches away from Node (1, 1). This phenomenon is because Node (2, 2) has two incoming EMWs, whereas Node (1, 3) has one incoming EMW and two outgoing EMWs. Another example is that the travel time from Node (1, 1) to Node (1, 10) is 0.532 s, whereas that from Node (1, 10) to Node (10, 10) is 0.190 s. Thus, in a 2-D square system, the EMW from a disturbance starting at one corner may travel at some nominal speed initially but would accelerate when approaching the opposite corner.

Also, the average EMW propagation speed along the boundaries is not the same as that across the diagonal. Table 2 shows that the propagation time across the diagonal is 0.722 s, corresponding to the speed of 1.959 pu-length/s based on the diagonal length of $\sqrt{2}$. Thus, the predicted speed c is within 4.65% of error of the measurement across the diagonal.

B. Florida Event Replication on the 2-D System

To support the 2-D system EMW propagation, this section studies the wave propagation of the 2008 Florida generator-load trip event [4] using the proposed 2-D uniform system. From the recorded data [4], the EMW took approximately 2 s to propagate from Florida to Manitoba. The event is simulated with ANDES [29] in the large-scale testbed [30] using the CURENT ERC EI reduced-order model [31] with a load-shedding event at 1 s. The frequencies at several locations in the system are shown in Fig. 22. Compared to the measured PMU data for the real event (see [23, Fig. 10.16]), although the maximum frequency deviations are different, the simulated frequency response show qualitative similarity with the EMW arriving first in Tennessee and subsequently in Manitoba, where the EMW takes 2.162 s to arrive.

The event is replicated approximately in the uniform 2-D system by selecting the appropriate machine inertia and line impedance, where Node (1, 1) represents Florida and Node (10, 10) represents Manitoba. The calculation of the equivalent impedance and inertia are provided in Appendix C. The simulation performed with the equivalent parameters but a smaller disturbance is shown in Fig. 23. For the frequency threshold of 60.002 Hz, the load trip event at 1 s arrives at Bus (1, 1) at 1.20 s and Bus (10, 10) at 2.996 s, yielding a propagation time of 1.796 s. This

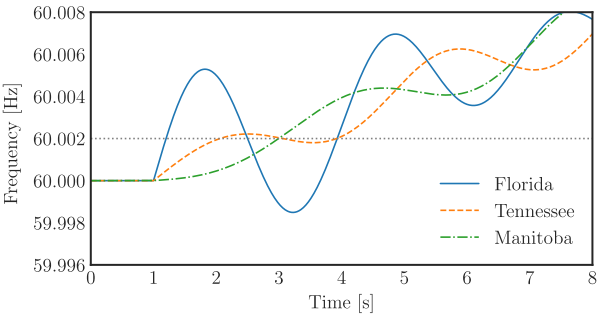

Fig. 23. ***EMW propagation in the 2-D system replicating the Florida event.***

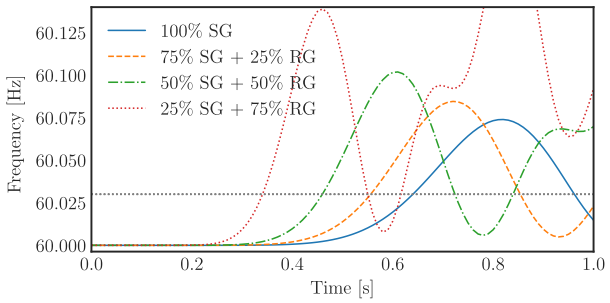

Fig. 24. *Frequency at Bus (1, 10) of the 2-D system for different renewable levels.*

propagation time is within 17.0% of the reduced EI system propagation time. The ability of the 10×10 2-D system to approximate the propagation speed is encouraging as the reduction of the EI system to the 10×10 system is quite drastic.

C. Cases With Converter-Interfaced Renewable Resources

Now, the impact of renewable resource penetration is simulated for the 2-D system with the load trip disturbance and the SG and inverter pairing, as shown in Fig. 21. The frequencies of Bus (1, 10) in 2-D systems with renewable levels $\rho = 0.25$, 0.5, and 0.75 are shown in Fig. 24. For the threshold of 60.03 Hz, the same threshold as in the base case, the EMW propagation time from Bus (1, 1) to Bus (1, 10) is 0.449, 0.355, and 0.238 s for the three renewable scenarios, compared with 0.532 s for the base case. The propagation time to Bus (10, 10) in the three scenarios are 0.616, 0.493, and 0.337 s compared to 0.722 s in the base case.

As expected, the EMW propagation speeds up as the ratio of renewables increases. While the prediction formula is the same as for the 1-D system, namely, the speed is inversely proportional to the square root of the SG inertia, the propagation speed in the $\rho = 0.75$ scenario is faster than twice that of the original case. The observation reflects the complexity of predicting the propagation speed in a 2-D system.

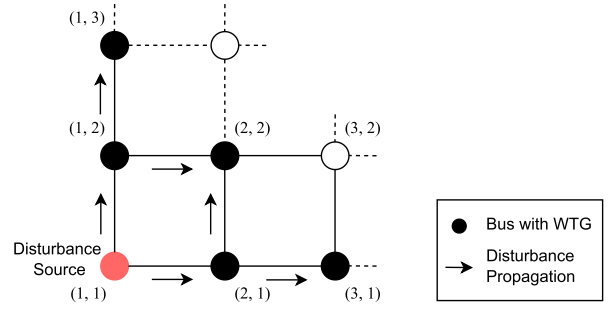

Fig. 25. *2-D system layout around Bus (1, 1) and WTG placement.*

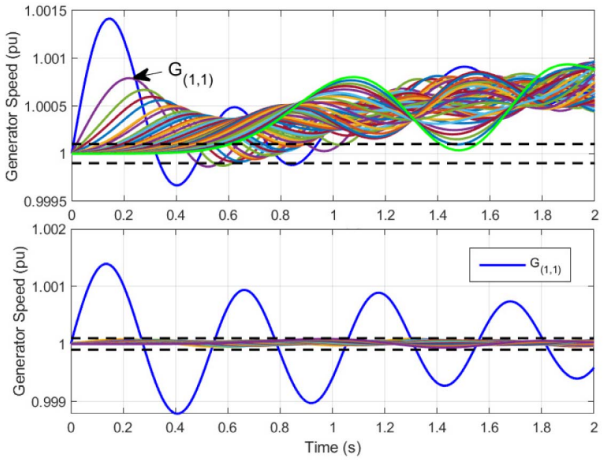

Fig. 26. *Frequency wave propagation without (top) and with (bottom) active power flow control.*

VIII. DISTURBANCE ATTENUATION IN 2-D SYSTEMS

This section demonstrates the efficacy of the flow control discussed in Section V to the attenuation of disturbance propagation in the 2-D network in Fig. 18. The base system is assumed to have SGs on each bus. The power system is dispatched so as to transfer 100 MW from Bus (1, 1) to Bus (10, 10). In addition, a 50-MW load is connected to Bus (1, 1), which is disconnected at $t = 0$ s. For the same event, we replace five SG units on Buses (1, 2), (1, 3), (2, 1), (2, 2), and (3, 1) with WTGs of the same rating. The WTGs are dispatched to output 80 MW, which are consumed locally by constant-power loads. The buses hosting WTGs are denoted by solid dots in Fig. 25. Each WTG is controlling the incoming active power flows (the sum of them if more than one) as indicated by the arrows.

The SG speeds across the system are shown in Fig. 26. The top figure corresponds to the base case of no convert-

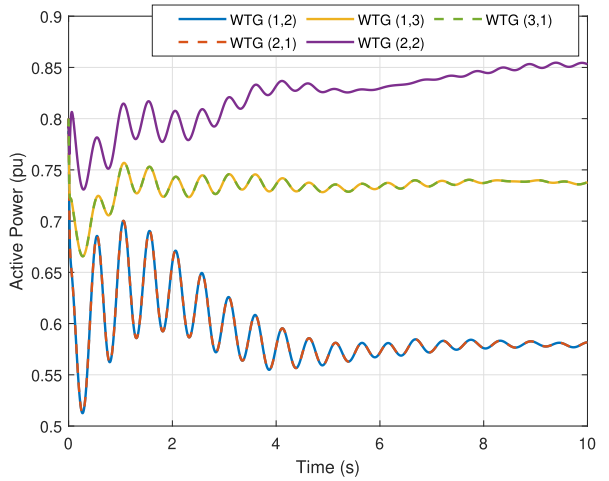

Fig. 27. *Wind turbine active power outputs.*

ers and the bottom corresponds to five WTGs employing the active line flow power control. In the base case, the propagation time is 0.61 s, whereas with the integration of the line flow control, the propagation of the disturbance virtually stops at the buses of the WTGs, as no oscillations are visible on rotor speeds of the machines across the system. The active power response of the WTG plants can be noted in Fig. 27. WTGs (1, 2) and (2, 1) immediately adjust their output to accommodate the excess 0.25-pu flow on the transmission lines due to the load trip. In the meantime, they counter the active power deviations by effectively containing the oscillation on the tie line. Thus, the next tie lines have significantly less oscillations such that the disturbance is not visible three buses away.

IX. CONCLUSION

High penetration of converter-interfaced renewables will reshape the swing dynamics in future power systems. As demonstrated in the uniform 1-D and 2-D systems, GFL converters that replace part of the SG capacity will speed up the EMW propagation due to the reduced inertia, following the proposed prediction formula. GFL converters controlled as VSGs with inertia emulation can slow down the EMW propagation, but converter response needs to be increased to restore the propagation speed. Converters with fast active power control can mitigate the EMW propagation or even block it when assisted with reactive power damping control, which is highly effective as demonstrated in both 1-D and 2-D systems. Therefore, even as the converters speed up the propagation of EMW, advanced controls show promise in restoring the propagation speed. ■

ACKNOWLEDGMENT

The authors would like to thank Dr. Yichen Zhang for the discussions on converter modeling and simulation.

APPENDIX

A. Derivation of the EMW Equation for the 2-D System

Consider the dynamics of the generator on Bus (i, j). After neglecting the damping effect, the rotor angle $\delta_{i,j}$ follows:

$$\dot{\delta}_{i,j} = \Omega(\omega_{i,j} - \omega_n)$$

where ω_n is the nominal angular speed. Taking its partial derivative with respect to time yields

$$\ddot{\delta}_{i,j} = \Omega\dot{\omega}_{i,j} \Rightarrow \dot{\omega}_{i,j} = \frac{\ddot{\delta}_{i,j}}{\Omega}. \tag{A.1}$$

The motion of the synchronous machine (i, j) is determined by

$$M\dot{\omega}_{i,j} = P_{m,i,j} - P_{e,i,j} \tag{A.2}$$

where $P_{m,i,j}$ is the constant mechanical power input and $P_{e,i,j}$ is the electrical power output. Combine (A.1) and (A.2) to obtain

$$\frac{M}{\Omega}\ddot{\delta}_{i,j} = -P_{e,i,j}. \tag{A.3}$$

For an interior Bus (i, j), the outgoing electrical power has two directions: $P_{(i,j),(i+1,j)}$ and $P_{(i,j),(i,j+1)}$. Similarly, the incoming power are $P_{(i-1,j),(i,j)}$ and $P_{(i,j-1),(i,j)}$. Therefore, the power provided by the generator is given by

$$\begin{aligned} P_{e,i,j} = &\left(P_{(i,j),(i+1,j)} - P_{(i-1,j),(i,j)}\right) \\ &+ \left(P_{(i,j),(i,j+1)} - P_{(i,j-1),(i,j)}\right) \end{aligned} \tag{A.4}$$

which is the power balance equation at Bus (i, j), an alternative to the current balance equation used in [3]. Apply the dc power flow equation to (A.4) to obtain

$$\begin{aligned} P_{(i,j),(i+1,j)} &= (\delta_{i,j} - \delta_{i+1,j})/X \\ P_{(i-1,j),(i,j)} &= (\delta_{i-1,j} - \delta_{i,j})/X \\ P_{(i,j),(i,j+1)} &= (\delta_{i,j} - \delta_{i,j+1})/X \\ P_{(i,j-1),(i,j)} &= (\delta_{i,j-1} - \delta_{i,j})/X \end{aligned} \tag{A.5}$$

where X is the reactance between two adjacent buses.

Substituting (A.5) into (A.4) yields

$$\begin{aligned} XP_{e,i,j} = &(\delta_{i,j} - \delta_{i+1,j}) - (\delta_{i-1,j} - \delta_{i,j}) \\ &+(\delta_{i,j} - \delta_{i,j+1}) - (\delta_{i,j-1} - \delta_{i,j}). \end{aligned} \tag{A.6}$$

For an infinitesimal change Δx in the first dimension

$$\left.\frac{\partial\delta}{\partial x}\right|_{i,j} \approx (\delta_{i+\Delta x,j} - \delta_{i,j})/\Delta x. \tag{A.7}$$

Let $\Delta x = l$, which is the length between two neighboring generators. The subscript $i + \Delta x$ becomes $i + 1$ and

$$(\delta_{i+1,j} - \delta_{i,j}) \approx l \left.\frac{\partial\delta}{\partial x}\right|_{i,j}. \tag{A.8}$$

Likewise,

$$(\delta_{i,j} - \delta_{i-1,j}) \approx l \left.\frac{\partial\delta}{\partial x}\right|_{(i-1),j}. \tag{A.9}$$

Repeat the approximation for the remaining two terms in (A.6), and one can obtain

$$P_{e,i,j} = -k\left(\left.\frac{\partial\delta}{\partial x}\right|_{i,j} - \left.\frac{\partial\delta}{\partial x}\right|_{(i-1),j} + \left.\frac{\partial\delta}{\partial y}\right|_{i,j} - \left.\frac{\partial\delta}{\partial y}\right|_{i,(j-1)}\right) \tag{A.10}$$

where $k = (dX/d\ell)^{-1}$.

Apply finite differences to obtain the approximations of $\partial^2\delta/\partial x^2$ and $\partial^2\delta/\partial y^2$ as

$$\left.\frac{\partial^2\delta}{\partial x^2}\right|_{i-1,j} \approx \left(\left.\frac{\partial\delta}{\partial x}\right|_{i-1+\Delta x,j} - \left.\frac{\partial\delta}{\partial x}\right|_{i-1,j}\right)/\Delta x \tag{A.11}$$

$$\left.\frac{\partial^2\delta}{\partial y^2}\right|_{i,j-1} \approx \left(\left.\frac{\partial\delta}{\partial y}\right|_{i,j-1+\Delta y} - \left.\frac{\partial\delta}{\partial y}\right|_{i,j-1} \right)/\Delta y. \quad \text{(A.12)}$$

In (A.11) and (A.12), let $\Delta x = \Delta y = l$. The subscripts $i-1+\Delta x$ and $j-1+\Delta y$ become i and j, respectively. Substitute (15) and (16) into (14) to obtain

$$P_{e,i,j} \approx -kl \left(\left.\frac{\partial^2\delta}{\partial x^2}\right|_{i-1,j} + \left.\frac{\partial^2\delta}{\partial y^2}\right|_{i,j-1} \right). \quad \text{(A.13)}$$

Assume that $\partial^2\delta/\partial x^2$ and $\partial^2\delta/\partial y^2$ are sufficiently smooth, and (A.13) can become an equality for point $i' \in (i-1, i)$ and $j' \in (j-1, j)$

$$P_{e,i,j} = -kl \left(\left.\frac{\partial^2\delta}{\partial x^2}\right|_{i',j} + \left.\frac{\partial^2\delta}{\partial y^2}\right|_{i,j'} \right). \quad \text{(A.14)}$$

For i' and j' in close proximity to i and j, respectively, (A.14) and (A.3) can be combined to obtain

$$\frac{M}{\Omega}\ddot{\delta}_{i,j} = P_{e,i,j} = kl \left(\left.\frac{\partial^2\delta}{\partial x^2}\right|_{i,j} + \left.\frac{\partial^2\delta}{\partial y^2}\right|_{i,j} \right). \quad \text{(A.15)}$$

Take the partial derivative of (A.15) with respect to l and rewrite it in compact notation to obtain the membrane equation

$$\ddot{\delta} = c^2 \left(\delta_{xx} + \delta_{yy}\right) \quad \text{(A.16)}$$

where $c^2 = k\Omega/m$, $m = dM/d\ell$, and $k = (dX/d\ell)^{-1}$. If all the quantities are in per unit on the same base, it can be observed from (A.16) that c has a dimension of pu-length/s.

B. Analytical Solutions for the 2-D EMW Equation

1) Separation of Variables: To solve (A.16), one can employ the standard separation of variables technique to obtain the Helmholtz equation. Assume that $\delta(x, y, t)$ is separable in space and time such that

$$\delta(x, y, t) = F(x, y)G(t). \quad \text{(A.17)}$$

Substitute (A.17) into (A.15) and rearrange to obtain

$$\frac{\ddot{G}}{c^2 G} = \frac{1}{F}(F_{xx} + F_{yy}). \quad \text{(A.18)}$$

Since there is no variable coupling, the two sides have to be equal to a constant, say, $-v^2$

$$\frac{\ddot{G}}{c^2 G} = -v^2, \quad \frac{1}{F}(F_{xx} + F_{yy}) = -v^2. \quad \text{(A.19)}$$

The first part of (A.19) can be written as

$$\ddot{G} + \lambda^2 G = 0 \quad \text{(A.20)}$$

where $\lambda = cv$, which is a linear ODE for an undamped oscillator. The second part

$$F_{xx} + F_{yy} + v^2 F = 0 \quad \text{(A.21)}$$

is a 2-D eigenvalue problem when combined with the boundary conditions. This 2-D Helmholtz equation can be solved with a further separation of variables as

$$F(x, y) = H(x)Q(y) \quad \text{(A.22)}$$

where

$$H_{xx} + k^2 H = 0, \quad Q_{yy} + p^2 Q = 0 \quad \text{(A.23)}$$

and $p^2 = v^2 - k^2$.

The separation of spatial and temporal variables allows the boundary conditions and initial conditions to be applied separately.

2) Boundary Conditions: The solutions to the Helmholtz equation in (A.23) take the form of

$$\begin{aligned} H(x) =& A\cos(kx) + B\sin(kx) \\ Q(y) =& C\cos(py) + D\sin(py), \quad k, p \in \mathbb{N}. \end{aligned} \quad \text{(A.24)}$$

The boundary conditions are derived in a way analogous to the wave problems with free boundaries. The mechanical wave of rotor angles will stop propagating once it reaches the edges, which means that the variation of rotor angles with respect to an infinitesimal change in displacement, in the wave direction, is zero at the edges. Without loss of generality, let a and b denote the length along the x-axis and y-axis, respectively, the boundary conditions can be written as in (17).

To obtain nontrivial solutions, namely, $H(x) \neq 0$, $Q(y) \neq 0$, and $G(t) \neq 0$, the boundary conditions are simplified into

$$H_x(0) = H_x(a) = Q_y(0) = Q_y(b) = 0. \quad \text{(A.25)}$$

Since

$$\begin{aligned} H_x &= -kA\sin(kx) + kB\cos(kx) \\ Q_y &= -pC\sin(py) + pD\cos(py) \end{aligned} \quad \text{(A.26)}$$

the boundary conditions (A.25) yields

$$B = D = 0, \quad k = \frac{m\pi}{a}, \quad p = \frac{n\pi}{b}. \quad \text{(A.27)}$$

Denoting

$$H_m(x) = A\cos\left(\frac{m\pi}{a}x\right), \quad Q_n(y) = C\cos\left(\frac{n\pi}{b}y\right) \tag{A.28}$$

the (m,n) term of the solution to the Helmholtz equation is

$$\begin{aligned} F_{m,n}(x,y) &= H_m(x)Q_n(y) \\ &= \Gamma \times \cos\left(\frac{m\pi}{L}x\right)\cos\left(\frac{n\pi}{L}y\right), \quad m,n \in \mathbb{N} \end{aligned} \tag{A.29}$$

where $\Gamma = AC$. Expression (A.29) is a family of solutions that satisfy the boundary conditions. Substitute (A.29) into the original Helmholtz equation (A.21) and compare the coefficients to obtain

$$v^2 = \left(\frac{m\pi}{a}\right)^2 + \left(\frac{n\pi}{b}\right)^2 \tag{A.30}$$

which is the condition required for (A.29) to be the solutions for (A.21).

3) Initial Conditions: Since $p^2 = v^2 - k^2$, the eigenvalue λ of (A.20) is given by $\lambda = cv = c(p^2+k^2)^{1/2}$.

Given that $k = m\pi/a$ and $p = n\pi/b$, introduce the indices m and n for λ to obtain

$$\lambda_{m,n} = c\pi\left[\left(\frac{n}{b}\right)^2 + \left(\frac{m}{a}\right)^2\right]^{1/2}, \quad m,n \in \mathbb{N} \tag{A.31}$$

where $\lambda_{m,n}$ are the eigenvalues of the system (A.20).

Thus, the general solution to $G(t)$ is

$$G_{m,n}(t) = B_{m,n}\cos(\lambda_{m,n}t) + B'_{mn}\sin(\lambda_{m,n}t) \tag{A.32}$$

where $B_{m,n}$ and B'_{mn} are determined by the boundary conditions.

4) Complete Solution: The solution for the (m,n) terms becomes

$$\begin{aligned} &\delta_{m,n}(x,y,t) \\ &= F_{m,n}(x,y)G_{m,n}(t) \\ &= \Gamma\cos\left(\frac{m\pi}{a}x\right)\cos\left(\frac{n\pi}{b}y\right) \\ &\quad \times \left[B_{m,n}\cos(\lambda_{m,n}t) + B'_{mn}\sin(\lambda_{m,n}t)\right], \quad m,n \in \mathbb{N}. \end{aligned} \tag{A.33}$$

The complete solution is a summation over the $\delta_{m,n}$ term

$$\delta(x,y,t) = \sum_{m=1}^{\infty}\sum_{n=1}^{\infty}\delta_{m,n}(x,y,t). \tag{A.34}$$

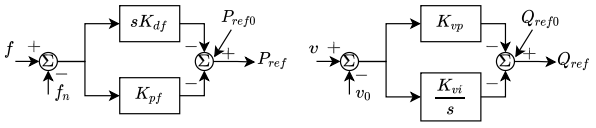

Fig. 28. *Outer loop reference generators for GFL converters. Left: frequency control loop. Right: voltage control loop.*

At $t = 0$, it should be equal to $f(x,y)$, and the initial rotor angle displacements

$$\begin{aligned} \delta(x,y,0) &= \sum_{m=1}^{\infty}\sum_{n=1}^{\infty}\Gamma B_{m,n}\cos\left(\frac{m\pi}{a}x\right)\cos\left(\frac{n\pi}{b}y\right) \\ &= f(x,y). \end{aligned} \tag{A.35}$$

To observe the EMW propagation in a system perturbed from steady state, all rotor angles can be assumed to be zero initially, i.e., $f(x,y) = 0$. Therefore,

$$B_{m,n} = 0. \tag{A.36}$$

At $t = 0$, generators' rotor angles can have an initial velocity to model the disturbance. Without loss of generality, the initial velocity is modeled by $g(x,y)$. The initial condition is thus

$$\delta_t(x,y,0) = g(x,y). \tag{A.37}$$

Since, for $m,n \in \mathbb{N}$,

$$\begin{aligned} \delta_t(x,y,0) &= g(x,y) \\ &= \sum_{m=1}^{\infty}\sum_{n=1}^{\infty}(\Gamma B'_{m,n}\lambda_{m,n})\cos\left(\frac{m\pi}{a}x\right)\cos\left(\frac{n\pi}{b}y\right). \end{aligned} \tag{A.38}$$

Denote

$$K_m(y) = \sum_{n=1}^{\infty}(\Gamma B'_{m,n}\lambda_{m,n})\cos\left(\frac{n\pi}{b}y\right) \tag{A.39}$$

which acts as the coefficients for the Fourier series of $g(x,y)$, namely,

$$K_m(y) = \frac{2}{a}\int_0^a f(x,y)\cos\left(\frac{n\pi}{a}x\right)dx. \tag{A.40}$$

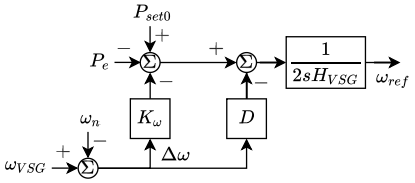

Fig. 29. *Outer loop for VSG control in GFL converters.*

The parameter $\Gamma B'_{m,n}\lambda_{m,n}$ in the coefficients of the Fourier series of $K_{m,n}(y)$ is being recursively determined as

$$\begin{aligned} B'_{m,n} &= \frac{2}{\Gamma b}\int_0^b K_m(y)\cos\left(\frac{n\pi}{b}y\right)dy \\ &= \frac{4}{ab\lambda_{m,n}\Gamma}\int_0^b\int_0^a f(x,y)\cos\left(\frac{n\pi}{a}x\right) \\ &\quad\times\cos\left(\frac{n\pi}{b}y\right)dxdy. \end{aligned} \tag{A.41}$$

Including the boundary and initial conditions, the complete solution is

$$\delta(x,y,t)=\sum_{m=1}^{\infty}\sum_{n=1}^{\infty}\Gamma B'_{m,n}\cos\left(\frac{m\pi}{a}x\right)\cos\left(\frac{n\pi}{b}y\right)\sin\left(\lambda_{m,n}\right) \tag{A.42}$$

for $m,n\in\mathbb{N}, t\geq 0$, where $\lambda_{m,n}=c\pi[(\frac{n}{b})^2+(m/a)^2]^{1/2}$. The main observation from (A.42) is that as the order m or n increases, the amplitude decreases due to $\lambda_{m,n}$ in the denominator.

C. Calculation of EI Model Equivalent Impedance and Inertia

This appendix extends the derivation in [2] for WECC equivalent parameters to those for EI. The total inertia in the CURENT EI model is 28 250 pu (on 100-MVA base) and is distributed evenly to 100 generators, that is, the equivalent inertia H at each node is 282.50 s. Based on the impedance between Florida and Tennessee, the impedance between Florida and Manitoba is scaled to

$$X_{\text{FL, MB}}=\frac{X_{\text{FL, TN}}}{l_{\text{FL, TN}}}l_{\text{FL, MB}}=\frac{0.03}{606}\times 2893=0.143\text{ pu} \tag{A.43}$$

where l is the distance in miles. The impedance between Manitoba and Florida is considered as the impedance across the diagonal of the 2-D system. Therefore, the impedance per branch in a 10×10 grid is

$$X=\frac{0.143}{9\sqrt{2}}=0.011\text{ pu}. \tag{A.44}$$

These H and X values are used in the 2-D system for the simulation of the Florida event in Section VII-B.

D. Reference Generators for GFL and GFM Converters

The outer loop reference generator for frequency and voltage controls in GFL converters is shown in Fig. 28. The outer loop controller for inertia emulation and power droop in GFM converters is shown in Fig. 29.

REFERENCES

[1] A. Semlyen, "Analysis of disturbance propagation in power systems based on a homogeneoue dynamic model," *IEEE Trans. Power App. Syst.*, vol. PAS-93, no. 2, pp. 676–684, Mar. 1974.

[2] R. L. Cresap and J. F. Hauer, "Emergence of a new swing mode in the western power system," *IEEE Trans. Power App. Syst.*, vol. PAS-100, no. 4, pp. 2037–2045, Apr. 1981, doi: 10.1109/TPAS.1981.316481.

[3] J. S. Thorp, C. E. Seyler, and A. G. Phadke, "Electromechanical wave propagation in large electric power systems," *IEEE Trans. Circuits Syst. I, Fundam. Theory Appl.*, vol. 45, no. 6, pp. 614–622, Jun. 1998.

[4] L. Vanfretti and J. H. Chow, "Analysis of power system oscillations for developing synchrophasor data applications," in *Proc. IREP Symp. Bulk Power Syst. Dyn. Control*, Buzios, Brazil, Aug. 2010, pp. 1–17.

[5] M. Parashar, J. S. Thorp, and C. E. Seyler, "Continuum modeling of electromechanical dynamics in large-scale power systems," *IEEE Trans. Circuits Syst. I, Reg. Papers*, vol. 51, no. 9, pp. 1848–1858, Sep. 2004.

[6] T. Li, G. Ledwich, Y. Mishra, J. H. Chow, and A. Vahidnia, "Wave aspect of power system transient stability—Part I: Finite approximation," *IEEE Trans. Power Syst.*, vol. 32, no. 4, pp. 2493–2500, Jul. 2017.

[7] T. Li, G. Ledwich, Y. Mishra, J. H. Chow, and A. Vahidnia, "Wave aspect of power system transient stability—Part II: Control implications," *IEEE Trans. Power Syst.*, vol. 32, no. 4, pp. 2501–2508, Jul. 2017.

[8] S. Sahyoun, S. M. Djouadi, K. Tomsovic, and S. Lenhart, "Optimal distributed control for continuum power systemsm" in *Proc. Conf. Control Appl.*, C. Bonnet, B. Pasik-Duncan, H. Ozbay, and Q. Zhang, Eds. Philadelphia, PA, USA: SIAM, 2015, pp. 416–422, doi: 10.1137/1.9781611974072.57.

[9] A. G. Phadke and J. S. Thorp, *Synchronized Phasor Measurements and Their Applications*. New York, NY, USA: Springer, 2008.

[10] S. You *et al.*, "Disturbance location determination based on electromechanical wave propagation in FNET/GridEye: A distribution-level wide-area measurement system," *IET Gener., Transmiss. Distrib.*, vol. 11, no. 18, pp. 4436–4443, 2017.

[11] A. Esmaeilian and M. Kezunovic, "Impact of electromechanical wave oscillations propagation on protection schemes," *Electr. Power Syst. Res.*, vol. 138, pp. 85–91, Sep. 2016.

[12] F. Milano, F. Dörfler, G. Hug, D. J. Hill, and G. Verbič, "Foundations and challenges of low-inertia systems," in *Proc. Power Syst. Comput. Conf. (PSCC)*, 2018, pp. 1–25.

[13] F. Wilches-Bernal, J. H. Chow, and J. J. Sanchez-Gasca, "A fundamental study of applying wind turbines for power system frequency control," *IEEE Trans. Power Syst.*, vol. 31, no. 2, pp. 1496–1505, Mar. 2016.

[14] J. Rocabert, A. Luna, F. Blaabjerg, and P. Rodríguez, "Control of power converters in AC microgrids," *IEEE Trans. Power Electron.*, vol. 27, no. 11, pp. 4734–4749, Nov. 2012, doi: 10.1109/TPEL.2012.2199334.

[15] S. Konstantinopoulos and J. H. Chow, "Dynamic active power control in type-3 wind turbines for transient stability enhancement," in *Proc. IEEE Power Energy Soc. Gen. Meeting (PESGM)*, Jul. 2021, pp. 1–5.

[16] R. Ofir, U. Markovic, P. Aristidou, and G. Hug, "Droop vs. virtual inertia: Comparison from the perspective of converter operation mode," in *Proc. IEEE Int. Energy Conf. (ENERGYCON)*, Limassol, Cyprus, Jun. 2018, pp. 1–6.

[17] *Solar Photovoltaic Power Plant Modeling and Validation Guideline*, WECC, Salt Lake City, UT, USA, 2019.

[18] Q.-C. Zhong and G. Weiss, "Synchronverters: Inverters that mimic synchronous generators," *IEEE Trans. Ind. Electron.*, vol. 58, no. 4, pp. 1259–1267, Apr. 2011.

[19] A. Tayyebi, D. Groß, A. Anta, F. Kupzog, and F. Dörfler, "Frequency stability of synchronous machines and grid-forming power converters," *IEEE J. Emerg. Sel. Topics Power Electron.*, vol. 8, no. 2, pp. 1004–1018, Jun. 2020.

[20] D. Osipov and J. H. Chow, "Operation paradigm for power systems with high penetration of renewables and effects of climate change," in *Proc. IEEE Power Energy Soc. Gen. Meeting (PESGM)*, Jul. 2021, pp. 1–4.

[21] D. Ramasubramanian, Z. Yu, R. Ayyanar, V. Vittal, and J. Undrill, "Converter model for representing converter interfaced generation in large scale grid simulations," *IEEE Trans. Power Syst.*, vol. 32, no. 1, pp. 765–773, Jan. 2017, doi: 10.1109/TPWRS.2016.2551223.

[22] P. W. Sauer, M. A. Pai, and J. H. Chow, *Power System Dynamics and Stability*, 2nd ed. Hoboken, NJ, USA: Wiley, 2018.

[23] E. V. Larson and J. H. Chow, "SVC control design concepts for system dynamic performance," in *Proc. IEEE PES Winter Power Meeting*, Jan. 1987, pp. 1–18.

[24] K. Clark, N. W. Miller, and J. J. Sanchez-Gasca, "Modeling of GE wind turbine-generators for grid studies," General Electr. Int., Inc., Schenectady, NY, USA, GE Tech. Rep., Aug. 2010.

[25] J. Morren, S. W. H. de Haan, W. L. Kling, and J. A. Ferreira, "Wind turbines emulating inertia and supporting primary frequency control," *IEEE Trans. Power Syst.*, vol. 21, no. 1, pp. 433–434, Feb. 2006.

[26] A. Tayyebi, F. Dörfler, F. Kupzog, Z. Miletic, and W. Hribernik, "Grid-forming converters—Inevitability, control strategies and challenges in future grids application," in *Proc. CIRED Ljublijana Workshop Microgrids Local Energy Communities*, 2018, pp. 1–5. [Online]. Available: https://www.cired-repository.org/handle/20.500.12455/1053

[27] B. C. Lesieutre, E. Scholtz, and G. C. Verghese, "Impedance matching controllers to extinguish

electromechanical waves in power networks," in *Proc. IEEE Int. Conf. Control Appl.*, vol. 1, Sep. 2002, pp. 25–30.

[28] K. F. Riley, M. Hobson, and S. J. Bence, *Mathematical Methods for Physics and Engineering*. Cambridge, U.K.: Cambridge Univ. Press, 1999, pp. 165–169.

[29] H. Cui, F. Li, and K. Tomsovic, "Hybrid symbolic-numeric framework for power system modeling and analysis," *IEEE Trans. Power Syst.*, vol. 36, no. 2, pp. 1373–1384, Mar. 2021, doi: 10.1109/TPWRS.2020.3017019.

[30] F. Li, K. Tomsovic, and H. Cui, "A large-scale testbed as a virtual power grid: For closed-loop controls in research and testing," *IEEE Power Energy Mag.*, vol. 18, no. 2, pp. 60–68, Mar. 2020, doi: 10.1109/MPE.2019.2959054.

[31] D. Osipov and M. Arrieta-Paternina. *Reduced Eastern Interconnection System Model*. Accessed: Nov. 5, 2022. [Online]. Available: https://curent.utk.edu/2016SiteVisit/EI_LTB_Report.pdf

[32] D. Pattabiraman, R. H. Lasseter., and T. M. Jahns, "Comparison of grid following and grid forming control for a high inverter penetration power system," in *Proc. IEEE Power Energy Soc. Gen. Meeting (PESGM)*, Aug. 2018, pp. 1–5, doi: 10.1109/PESGM.2018.8586162.

[33] A. Bykhovsky and J. H. Chow, "Power system disturbance identification from recorded dynamic data at the Northfield substation," *Int. J. Electr. Power Energy Syst.*, vol. 25, no. 10, pp. 787–795, Dec. 2003.

ABOUT THE AUTHORS

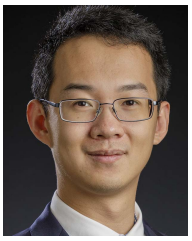

Hantao Cui (Senior Member, IEEE) received the B.S. and M.S. degrees from Southeast University, Nanjing, China, in 2011 and 2013, respectively, and the Ph.D. degree from The University of Tennessee, Knoxville, TN, USA, in 2018, all in electrical engineering.

He is currently an Assistant Professor with the School of Electrical and Computer Engineering, Oklahoma State University, Stillwater, OK, USA. His research interests include power system modeling, simulation, and high-performance computing.

Stavros Konstantinopoulos (Member, IEEE) received the Diploma degree in electrical and computer engineering from the National Technical University of Athens, Athens, Greece, in 2015, and the M.S. and Ph.D. degrees in electrical engineering from the Rensselaer Polytechnic Institute, Troy, NY, USA, in 2018 and 2021, respectively.

He is currently an Engineer II with the Grid Operations and Planning Group, Electric Power Research Institute, Palo Alto, CA, USA. His research interests include integration and control of renewable generation, transient stability analysis and control, power system monitoring, and phasor measurement unit (PMU) applications.

Denis Osipov (Member, IEEE) received the B.S. and M.S. degrees in electrical engineering from Donetsk National Technical University, Donetsk, Ukraine, in 2004 and 2005, respectively, and the Ph.D. degree in electrical engineering from The University of Tennessee Knoxville, Knoxville, TN, USA, in 2018.

He is currently a Research Scientist with the Department of Electrical, Computer, and Systems Engineering, Rensselaer Polytechnic Institute, Troy, NY, USA. His research interests include power system stability, modeling, and monitoring.

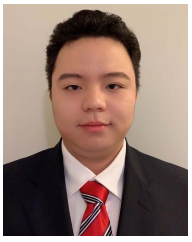

Jinning Wang (Graduate Student Member, IEEE) received the B.S. and M.S. degrees in electrical engineering from the Taiyuan University of Technology, Taiyuan, China, in 2017 and 2020, respectively. He is currently working toward the Ph.D. degree in electrical engineering at The University of Tennessee, Knoxville, TN, USA.

His research interests include demand response for frequency regulation, renewable integration, and power system control.

Fangxing (Fran) Li (Fellow, IEEE) received the B.S.E.E. and M.S.E.E. degrees from Southeast University, Nanjing, China, in 1994 and 1997, respectively, and the Ph.D. degree from Virginia Tech, Blacksburg, VA, USA, in 2001.

He is currently the James W. McConnell Professor in electrical engineering and the Campus Director of CURENT with the University of Tennessee, Knoxville, TN, USA. His current research interests include renewable energy integration, demand response, distributed generation and microgrid, energy markets, and power system computing.

Dr. Li has received a number of awards and honors, including the R&D 100 Award in 2020, the IEEE PES Technical Committee Prize Paper Award in 2019, the three best paper awards at international journals, and the six best papers/posters at international conferences. He was the Past Chair of IEEE PES Power System Operation, Planning and Economics (PSOPE) Committee from 2020 to 2021. Since 2020, he has been serving as the Editor-In-Chief of IEEE OPEN ACCESS JOURNAL OF POWER AND ENERGY (OAJPE).

Kevin L. Tomsovic (Fellow, IEEE) received the B.S. degree from Michigan Technological University, Houghton, MI, USA, in 1982, and the M.S. and Ph.D. degrees from the University of Washington, Seattle, WA, USA, in 1984 and 1987, respectively, all in electrical engineering.

He was the Head of the Department of Electrical Engineering and Computer Science, The University of Tennessee, Knoxville, TN, USA, from 2008 to 2013. He was on the Faculty of Washington State University, Pullman, WA, USA, from 1992 to 2008. He was the Advanced Technology for Electrical Energy Chair with Kumamoto University, Kumamoto, Japan, from 1999 to 2000. He was the NSF Program Director of the Electrical and Communications Systems Division, Engineering Directorate, from 2004 to 2006. He is currently a Chancellor's Professor with the Department of Electrical Engineering and Computer Science (EECS), The University of Tennessee, where he also directs the NSF/DOE Engineering Research Center CURENT.

Joe H. Chow (Life Fellow, IEEE) received the M.S. and Ph.D. degrees from the University of Illinois at Urbana–Champaign, Champaign, IL, USA, in 1975 and 1977, respectively.

After working at the General Electric Power System Business, Schenectady, NY, USA, he joined the Rensselaer Polytechnic Institute, Troy, NY, USA, in 1987, where he is currently an Institute Professor of electrical, computer, and systems engineering. His research interests include power system dynamics and control, flexible ac transmission system (FACTS) controllers, and synchronized phasor data.

Dr. Chow is also a member of the U.S. National Academy of Engineering. He was a past recipient of the IEEE PES Charles Concordia Power Engineering Award.